Supplementary Information: Massive volcanism, evaporite deposition, and the chemical evolution of the Early Cretaceous ocean

Jennifer V. Mills, Maya L. Gomes, Brian Kristall, Bradley B. Sageman, Andrew D. Jacobson, and Matthew T. Hurtgen*

Earth and Planetary Sciences, Northwestern University, Evanston, IL 60208, USA

* correspondence and requests for materials should be addressed to M.T.H.: matt@earth.northwestern.edu

Supplementary Methods

Carbonate Associated Sulfate (CAS) extraction and sulfur isotope analysis

Carbonate-associated sulfate (CAS) was extracted following a procedure adapted from Gill et al. (2011). A series of washes was performed on powdered samples in order to remove other forms of sulfate that could contaminate the CAS signal (i.e. gypsum, anhydrite, and organic sulfur). In brief, carbonate samples (25-100 grams) were crushed to a homogeneous powder in a shatterbox with an alumina ceramic vessel. Approximately 40 to 80 grams (~60 grams on average) of the powder from each sample was immersed in 400mL of a 10% NaCl solution, agitated for 10 minutes using a magnetic stirbar, and allowed to soak for 24 hours. The NaCl solution was then removed via vacuum filtration and samples were immersed in 1 L deionized water and agitated. The samples were allowed to soak for 24 hours, after which the overlying solution was removed by vacuum filtration. This step was performed twice for each sample following the NaCl leach. Samples were then immersed in 200 mL of 4% NaOCl solution, agitated, and allowed to soak for 48 hours. This NaOCl leach was performed three times for each sample, following which samples were rinsed with deionized water as described above (3x). Samples were then reacted with an excess of 3N HCl, to dissolve the carbonate matrix and liberate CAS. The resulting solution was separated from the insoluble residue via vacuum filtration (45μm). Approximately 25mL of a saturated solution of $BaCl_2$ (250g/L) was added to the filtrate to precipitate barium sulfate (barite, $BaSO_4$), and samples were allowed to sit at room temperature for at least two days to ensure complete precipitation. The barite was then collected via vacuum filtration (45μm), rinsed with 6N HCl and deionized water, and allowed to dry. Barite precipitates were homogenized and loaded into tin capsules with excess (approx. 2μg) V_2O_5 and analyzed for their $^{32/34}S$ ratios using a Thermo Delta-V-Plus isotope ratio mass spectrometer. Sulfur isotope results are reported as per mil (‰) deviations from the sulfur isotope composition of Vienna Cañon Diablo Troilite (VCDT). Sulfur isotope results were reproducible within ±0.2‰, based on repeat analysis of standards.

Carbon and oxygen isotopes

Micritic portions of bulk carbonate samples were microdrilled for carbon and oxygen isotope analysis. In cases where samples were entirely skeletal limestone, bivalve shells were targeted for isotope analysis. The drilled carbonate powder was reacted for 24 hours at room temperature (25°C) with 100% H_3PO_4 under helium atmosphere, and the released CO_2 was measured using a

Thermo Gas Bench coupled to a Thermo Delta V Plus continuous-flow isotope ratio mass spectrometer at Northwestern University. Carbon isotope results are reported as permil (‰) deviations from the carbon isotope composition of VPDB standard. Carbon isotope results were reproducible within ±0.1‰, based on repeat analysis of standards.

Site description

Carbonate samples spanning the OAE1a interval were obtained from a core drilled at Resolution Guyot in the Mid-Pacific Mountains (ODP Site 866) as part of Leg 143 of the Ocean Drilling Program. The core represents a 1600m shallow-water carbonate sequence, accumulated at a prolific rate atop an extinct volcanic seamount from ~130Ma until its drowning at around the Albian-Cenomanian boundary (Pringle and Duncan, 1995; Jenkyns and Wilson, 1999; Jones and Jenkyns, 2001). Recovered core sections are nearly 100% calcite and exhibit shallow-water platform and lagoonal facies, dominated by oolitic/peloidal grainstone, cyanobacterial laminite, and mudstone-wackestone carbonate interspersed with skeletal components (rudists, gastropods, and corals) (Jenkyns and Strasser, 1995; Strasser et al., 1999). OAE1a is recorded in the carbonate sequence as an immature, ~10cm thick, layer of marine laminated green to black carbon-rich shales stratigraphically coincident with the positive carbon isotope excursion characteristic of the Livello Selli event (Arnaud et al., 1995). The carbonate sequence represents a remarkably complete record of the period leading up to and through the OAE1a interval (~1200-450 mbsf of the core), although evidence from strontium isotope stratigraphy and lithologic data suggest the presence of an incomplete sedimentary record in the upper 450 meters of the core (Jenkyns et al., 1995; Jenkyns and Wilson, 1999). Despite initial interpretations of subaerial exposure and associated meteoric-water diagenesis (Röhl and Strasser, 1995), more recent work suggests little evidence exists for significant meteoric-water diagenesis (Wilson et al., 1998; Jenkyns and Wilson, 1999). The excellent correlation of the OAE1a carbon-isotope curve with other global sections also suggests minimal diagenesis of these isotope records (Menegatti et al., 1998; Bralower et al., 1999; Herrle et al., 2004; Luciani et al., 2006; Mehay et al., 2009). $\delta^{13}C_{carb}$, $\delta^{18}O_{carb}$, $\delta^{34}S_{sulfate}$ and $^{87}Sr/^{86}Sr$ are plotted alongside stratigraphy in Figure S1.

Age assignment of key core depths of Resolution Guyot ODP Hole 866A:

We utilize magnetostratigraphy (Fig. S2), benthic foraminifera biostratigraphy, carbon (Fig. S3) and strontium (Fig. S4) isotope stratigraphy, lithostratigraphy, and sequence stratigraphy in order to revise the age model for Resolution Guyot ODP Hole 866A in line with GTS2012 (Arnaud et al., 1995; Arnaud-Vanneau and Sliter, 1995; Jenkyns et al., 1995; Tarduno et al., 1995; Menegatti et al., 1998; Malinverno et al., 2010; McArthur et al., 2012; Ogg, 2012; Ogg and Hinnov, 2012). The key data points used for this revised age profile are listed and numbered in Table S1 with their new age assignments. Here, we provide detailed information about these key data; details on assigning ages and estimated uncertainty are provided in the following section.

The transition from the volcanic basement of Resolution Guyot to the start of carbonate sedimentation occurs in the top section of core 171 at 1619.3 mbsf. Initial facies evolution and sequence stratigraphy by Arnaud et al. (1995) identified the first 220m of sediment as a single lithologic unit consisting of oolitic and oncolytic limestones with significant dolomitization. This

section ends in core 148 at 1400.35 mbsf with a change from limestone to mudstone that contains algal mats and stromatolites. This change has been identified as a major sequence boundary that is thought to correspond to an emersion level (Arnaud et al., 1995). Arnaud-Vanneau and Sliter (1995) have assigned a Hauterivian age to this section based on benthic foraminifera. The consistent presence of *Vercorsella wintereri* and *Valvulineria* sp. from the top of core 171 to core 148 along with *Decussolocullina mirceai* in cores 171-167 is taken to indicate an Early Hauterivian age for this entire section. The assignment of an Early Hauterivian age for this entire section is further supported by correlation of the massive sequence boundary in core 148 to the megacycle regression of Ha5 (see Arnaud et al., 1995 and Ogg and Hinnov, 2012, Table S1 – **Datum 3**). This places the entire section (220 m of carbonate) precipitating within ≤2 Myrs from ~134-132 Ma. Such a large amount of carbonate deposition during the short time frame of the Early Hauterivian is consistent with other massive carbonate sections in the Tethys region at this time (Swiss Alps Alvier region 500 m of carbonate in ≤1 myr and Vocontian Basin 2 km of limestone-marl in 5 myr)(van de Schootbrugge et al., 2000).

In the GTS2012, the Ha5 megacycle regression occurs within M7r of the magnetostratographic M-series. Tarduno et al. (1995) identified 10 polarity zones (5 pairs of normal and reversed) based on 78 characteristic magnetization measurements in the lower 600 meters of sediment (Fig. S2). Tarduno et al. (1995) identified a change from reversed to normal polarity (J-/J+) at 1396 mbsf, just a few meters above the sequence boundary in the lower part of core 148 and the end of lithologic unit VIII (see Fig. 4 of Arnaud et al., 1995). Arnaud et al. (1995) characterize the lithologic units following this massive sequence boundary as representative of shallow subtidal and supratidal environments. Within this section (cores 148-103; ~1400-975 mbsf), Arnaud et al. (1995) identified algal-microbial mats, paleosols, desiccation cracks, subaerial exposure and sabkha parasequences. Considering these features, the magnitude of the Ha5 megacycle regression and identification of the sequence boundary as an emersion level in Hole 866A, it is reasonable to assume that there was erosion of sediment and/or a gap in sedimentation producing a minor unconformity. Needing to place this initial ~220 m of carbonate within the Early Hauterivian below M7r, it is reasonable to correlate the L-/L+ polarity transition at 1594.5 mbsf as the M10r-M10n transition of GTS2012, which is identified as the Hauterivian-Valanginian boundary with an age of 133.88 ± 0.6 Ma (Fig. S2 and Table S1 – **Datum 1**)(Tarduno et al., 1995; Ogg, 2012). This leads to K-/K+ corresponding to M9r and M9n, with the end of K+ (M9n) at 1441.4 mbsf representing an age of 133.05 ± 0.6 Ma (Fig. S2 and Table S1 – **Datum 2**)(Tarduno et al., 1995; Ogg, 2012). Taking into account the suspected unconformity produced by Ha5, the J- polarity zone is thought to correspond to M8r-M6r with M8n, M7 and parts of both M8r and M6r missing. Following this alignment and assuming there were no other major gaps in sedimentation, this would result in the large polarity zone of H- (1218.7-1054.2 mbsf) corresponding to M3r, which lasts 1.49 myr and spans Early to Late Barremian in the GTS2012 (Fig. S2)(Tarduno et al., 1995; Ogg, 2012).

The magnetostratigraphic record from Hole 866A ends at ~1000 mbsf during a normal polarity event. The next reliable major tie point comes from $\delta^{13}C$ stratigraphy identifying the start of the positive carbon isotope excursion (CIE) associated with OAE1a (Figure S3)(Menegatti et al., 1998). The truncation of the magnetostratigraphic record well before the $\delta^{13}C$ stratigraphy tie point in combination with the lithological and sedimentological interpretations of Arnaud et al. (1995) leaves some uncertainty in the precise correlation of the H+ polarity zone (Arnaud et al., 1995).

The identification of subaerial exposures along with paleosols, desiccation cracks, and sabkha parasequences throughout this section (~1400-950 mbsf) results in a high probability for the presence of minor unconformities (Arnaud et al., 1995). While there is reasonable confidence in correlating the I+/H- polarity transition to M5n/M3r it is possible that the H- polarity zone represents M3r through to M1r with M3n completely missing instead of just M3r. Therefore, the H+ polarity zone could represent M3n, M1n, or M3n and M1n with M1r missing. Again the truncation of the magnetostratigraphic record precludes a definitive assignment. The lithostratigraphy and facies analysis suggesting a highly restricted environment with numerous subaerial exposures through this section (1200-1000 mbsf) support the preferred assignment of the H- polarity zone representing M3r-M1r with M3n missing.

Following this revised magnetostratigraphic correlation for Hole 866A, the M5n/M3r-M1r (I+/H-) boundary at 1218.7 mbsf was assigned an age of 130.6 ± 0.5 Ma (**Datum 5**) and the M3r-M1r/M1n (H-/H+) boundary at 1054.2 mbsf was assigned an age of 128.32 ± 0.5 Ma (Fig. S2 and Table S1 – **Datum 6**). The placement of M3r in Hole 866A allowed for an estimation of the Hauterivian-Barremian boundary at 1240 ± 2.5 mbsf (130.8 ± 0.5 Ma GTS2012 – **Datum 4**). As noted above, the next major reliable tie point comes from the $\delta^{13}C$ stratigraphy identifying the positive CIE associated with OAE1a. Using the $\delta^{13}C$ stratigraphy of this study, the peak of the negative CIE that precedes the positive CIE associated with OAE1a (labeled C3 in Menegatti et al., 1998) occurs at 821.6 mbsf (Fig. S3 and Table S1 – **Datum 7**)(Menegatti et al., 1998). Previously published $\delta^{13}C$ stratigraphy, however, has the peak of the negative CIE preceding the positive CIE associated with OAE1a occurring at 841.7 mbsf (Jenkyns, 1995). While this difference is notable it does not alter the age profile noticeably or the interpretations presented in this study. Therefore, to be consistent with our other data we use the $\delta^{13}C$ stratigraphy of this study (instead of Jenkyns, 1995). Correlation of the $\delta^{13}C$ stratigraphy from this study with that of Menegatti et al. (1998) results in assigning the start of the positive CIE associated with OAE1a (labeled C4) in Hole 866A to a depth of 819 ± 2 mbsf with an age of 125.4 ± 0.4 Ma (Figure S3 and Table S1 – **Datum 8**).

Within the section of Hole 866A containing the Early Aptian positive CIE there is a distinct lithologic change from oolitic grainstone to cyclic packstone/wackstone that has been identified as a potential sequence boundary (676.55 mbsf, core 73R-1 75 cm) [Unit V-IV and SB17, see Figure 4 of Arnaud et al., 1995]. Considering that Arnaud et al. (1995) identify this boundary as a possible change from open marine conditions to shallow subtidal restricted marine conditions it is proposed to represent a minor unconformity. Comparing the $\delta^{13}C$ stratigraphy of this study to that of Menegatti et al., (1998), it is believed that the unconformity at 676.55 mbsf occurs at the end of the C5 stage (Figure S3). Orbital tuning of the Early Aptian positive CIE by Malinverno et al., (2010) estimates the duration of the C4 and C5 stages to be 749 ± 80 kyr (Malinverno et al., 2010). Therefore, the base of the unconformity at 676.55 mbsf is assigned an age of 124.65 ± 0.425 Ma (Table S1 – **Datum 9**). An additional 25 kyr is added to the uncertainty from the radioisotope dating to account for the uncertainty from the cyclostratigraphy, correlation of the $\delta^{13}C$ stratigraphy and placement of the unconformity.

Continuing the correlation of the $\delta^{13}C$ stratigraphy from this study with that of Menegatti et al. (1998), the unconformity at 676.55 mbsf is believed to have removed stage C6 and most of stage C7 of the Early Aptian positive CIE (Figure 2)(Malinverno et al., 2010). According to the

astrochronology time scale for the Early Aptian CIE by Malinverno et al. (2010), stage C7 is the longest at 1.59 ± 0.07 Myr. It is estimated that approximately three fourths of stage C7 is missing (Malinverno et al., 2010). Therefore, the top of the unconformity at 676.55 mbsf is assigned an age of 123.15 ± 0.425 Ma (Table S1 – **Datum 9**). The end of the Early Aptian positive CIE associated with OAE1a in Hole 866A is believed to occur at 599.3 mbsf on the $\delta^{13}C$ stratigraphy from this study (Figure S3). Compared to the Roter Sattel Early Aptian section the C8 stage of the positive CIE is quite compressed in Hole 866A (Menegatti et al., 1998). According to Menegatti et al. (1998), the positive CIE associated with OAE1a ends within the planktonic foraminifera zone *Globigerinelloides algerianus*. The boundary between planktonic foraminifera zones *G. ferreolensis* and *G. algerianus* occurs at 122.17 ± 0.4 Ma according to GTS2012. Therefore, the end of the positive CIE in Hole 866A at 599.3 mbsf is assigned an age of 122.0 ± 0.5 Ma (Table S1 – **Datum 10**).

Core recovery in the upper 550 m of Hole 866A was extremely poor, rarely getting above 10% recovery (Shipboard Scientific Party Leg 142, 1993). Hence, the limited benthic foraminifera data for this section of the core are not very diagnostic (Arnaud-Vanneau et al., 1995). Considering that the shape of the Sr isotope stratigraphy from Hole 866A plotted against depth matches very well with the global Sr isotope curve and the values from Hole 866A are reasonably within error of the global Sr isotope record, the LOWESS Fit 5 for the global Sr isotope record from GTS2012 was used to provide age constraints for the Late Aptian and Middle Albian (Fig. S4)(Jenkyns et al., 1995; Ogg and Hinnov, 2012). The global Sr isotope record reaches a minimum during the Late Aptian with a $^{87/86}Sr$ value of 0.707203 (Ogg and Hinnov, 2012). Using the LOWESS Fit 5 the age span of this minimum is estimated to be 115.25-114.90 Ma. In Hole 866A the $^{87/86}Sr$ minimum value of 0.707229 occurs at 434.43 mbsf. Taking into account the surrounding samples and their $^{87/86}Sr$ values, it is postulated that the sample at 434.43 mbsf would be located above the global minimum along the Late Aptian-Albian rising arm of the Sr isotope record. Therefore, this sample is assigned an age of 114.15 ± 0.55 Ma (Table S1 – **Datum 11**).

The Late Aptian-Albian rise in the global Sr isotope record reaches a plateau in the Middle Albian that continues through most of the Cenomanian (Ogg and Hinnov, 2012). This plateau with a $^{87/86}Sr$ value of 0.707420±15 is estimated to begin at 108.70 Ma according to the LOWESS Fit 5 (Ogg and Hinnov, 2012). In Hole 866A, the $^{87/86}Sr$ value of 0.707395 at 343.23 mbsf is thought to be representative of the start of the Albian-Cenomanian Sr isotope plateau. Therefore, this sample is assigned an age of 109.4 ± 0.7 Ma (Table S1 – **Datum 12**).

Based on the limited benthic foraminifera data Arnaud-Vanneau and Sliter (1995) loosely identify the Late Albian within the core catcher sample from core 15 (125-134.7 mbsf) and the remainder of the hole (Arnaud-Vanneau et al., 1995). With considerable uncertainty a Late Albian tie point is defined at 130 ± 15 mbsf with an age of 104.0 ± 0.5 Ma in order to provide additional constraint for the dating of the remainder of the drill hole (Table S1 – **Datum 13**).

Construction of age model and estimation of uncertainty

A number of different periods of constant sedimentation rate were assumed in the construction of the age model (Table S2). Despite sedimentological evidence suggesting minor gaps and variable sedimentation rates throughout the Barremian section of Hole 866A, the limited tie points within

this portion left no option but to assume constant sedimentation. Therefore, multiple different constant sedimentation rates were used to calculate ages for this section of Hole 866A. For these samples the average and standard deviation of the ages is the assigned age with 1σ error. For all other samples the error is propagated from the uncertainty in the age assignment and placement of the key tie points.

Coupled S-Sr cycle box model

Initial parameters for the sulfur-strontium box model are summarized in Table S3 and the input/output fluxes used to drive the model are summarized in Figure S5. In addition to the basic model described in the manuscript, additional complexity was added to explore specific scenarios. In particular, Wortmann and Chernyavski (2007) argue that massive evaporite (calcium sulfate) burial in the Early Cretaceous lowered marine sulfate concentrations thereby lowering global pyrite burial rates. Intuitively, if sulfate concentrations are low enough, rates of microbial sulfate reduction will decrease and less pyrite will be buried. However, microbial sulfate reduction has been shown to continue at quite low sulfate concentrations (Gomes and Hurtgen, 2013), so the exact shape of the pyrite burial-sulfate concentration curve and the threshold sulfate concentration after which pyrite burial rates will substantially decrease remains under debate. Wortmann and Chernyavsky (2007) used a reactive transport model to develop a parameterization for the sulfate concentration-pyrite burial relationship, which we have used here to demonstrate the influence of a pyrite burial flux that decreases with decreasing sulfate concentration. In order to incorporate this relationship, additional sulfur mass-balance and isotope mass-balance equations were formulated:

$$\frac{dM_S}{dt} = hF_H^{Sr} + wF_W^{Sr} - F_{py}^S([SO_4^{2-}]) - F_{evap}^S$$

$$\frac{dR_{SW}^S}{dt} = \frac{hF_H^{Sr}(R_H^S - R_{SW}^S) + wF_W^{Sr}(R_W^S - R_{SW}^S) - \Delta_{py}F_{py}([SO_4^{2-}])}{M_S}$$

where $F_{py}([SO_4^{2-}])$ is the sulfate concentration-dependent pyrite burial flux, defined as (Wortmann and Chernyavsky, 2007; Wortmann and Paytan, 2012):

$$F_{py}([SO_4]) = \frac{a * F_{py}(SS) * [SO_4]}{b + [SO_4]}$$

where $[SO_4^{2-}]$ is the seawater sulfate concentration (mmol/L) defined using an ocean volume of $1.38 * 10^{18} m^3$, a = 1.0691, b = 1.8685 (Wortmann and Chernyavsky, 2007), and $F_{py}(SS)$ is the high-sulfate pyrite burial rate (taken here to be $0.9*10^{12}$ mol/yr (Wortmann and Paytan, 2012)). Note that this yields a pyrite burial flux in mol/yr. The impact of implementing a sulfate concentration dependence on the pyrite burial flux is shown in Figure S5 (panel D).

Supplementary Discussion

Fidelity of the $\delta^{34}S_{CAS}$ record

It is important to evaluate the extent to which the S isotope composition of carbonate-associated sulfate (CAS) faithfully records the S isotope composition of seawater at the time of carbonate precipitation. Multiple post-depositional processes may overprint the primary marine $\delta^{34}S_{sulfate}$ signal including pore-fluid oxidation of sedimentary sulfide (e.g., pyrite) to sulfate and authigenic carbonate formation in pore fluids influenced by microbial sulfate reduction. In fact, a single sample may be influenced by both of these processes. A recent study utilized a multi-collector inductively coupled plasma-source mass spectrometer to identify large S isotope variability among different carbonate phases in a single hand sample (Present et al., 2015). While previous studies suggest that other geochemical proxies ($\delta^{13}C_{carb}$ and $^{87}Sr/^{86}Sr$) recorded in Site 866 samples are faithfully recording Early Cretaceous seawater chemistry (Wilson et al., 1998; Jenkyns and Wilson, 1999), it is worth discussing the S isotope record in more detail.

First, the carbon and oxygen isotope composition of marine carbonate can provide insight into the degree to which geochemical alteration has impacted ancient samples. For example, post depositional alteration resulting from isotopic exchange with meteoric and/or hydrothermal fluids may promote ^{13}C- and ^{18}O-depleted signatures as a consequence of carbonate dissolution and reprecipitation. However, carbon concentrations within these fluids are typically low, and therefore, $\delta^{13}C$ is often buffered to rock values. And, in fact, the Resolution Guyot samples exhibit considerable $\delta^{13}C$ and $\delta^{18}O$ scatter (Fig. S1). However, there is no obvious relationship between $\delta^{13}C$ and $\delta^{18}O$ and the $\delta^{13}C$ record is consistent with carbon isotope results from geographically distributed sections (Menegatti et al., 1998; Fig. S3). Therefore, while $\delta^{18}O$ was likely affected to some degree by post burial alteration, it appears that the $\delta^{13}C$ record is broadly recording a primary marine signal.

The $\delta^{34}S_{CAS}$ record can be split into three different sections (Fig. S1): (1) the interval leading up to the negative $\delta^{34}S_{CAS}$ shift (~1200 to 800 mbsf); (2) the negative $\delta^{34}S_{CAS}$ shift itself (~800 to 500 mbsf); and (3) the positive $\delta^{34}S_{CAS}$ shift (~500 to 0 mbsf). Interval 1 is characterized by significant $\delta^{34}S_{CAS}$ scatter. While this scatter likely reflects an element of post-burial alteration, we note that the average S isotope composition of carbonate through this interval is ~19‰, which is consistent with the $\delta^{34}S_{barite}$ record (Paytan et al., 2004). The most important part of the record for the interpretations made in the manuscript is Interval 2. Here, the $\delta^{34}S_{CAS}$ record is characterized by a systematic negative $\delta^{34}S_{CAS}$ shift (with minor scatter) that tracks the $\delta^{34}S_{barite}$ record (Paytan et al., 2004). Therefore, we argue Interval 2 is faithfully recording the S isotope evolution of Early Cretaceous seawater.

Interval 3 is characterized by a positive $\delta^{34}S_{CAS}$ shift but also considerable scatter. In fact, while the positive $\delta^{34}S_{CAS}$ shift of Site 866 does shift sympathetically with $^{87}Sr/^{86}Sr$, its initiation precedes the origination of the positive $\delta^{34}S_{barite}$ (Paytan et al., 2004) shift by ~10 Ma (compare Fig. 1 to Fig. 2). One possibility is that the S isotope discrepancy between $\delta^{34}S_{sulfate}$ data (our CAS vs. Paytan et al. (2004) barite) is simply a temporal reconstruction issue. However, the relationship between S and Sr isotopes are different in separate localities. For example, at Site

766 (Indian Ocean), $^{87}Sr/^{86}Sr$ rebounds to pre-excursion values before $\delta^{34}S_{barite}$ does (Fig. S6, Paytan et al., 2004 and Mearon et al., 2003). However, the $\delta^{34}S_{sulfate}$ data we generated from Resolution Guyot shift sympathetically with the $^{87}Sr/^{86}Sr$ (Fig. 3). The Sr isotope record through the Cretaceous has proven to be robust and reproducible in time and space (i.e., Jones and Jenkyns, 2001). Therefore, if the discrepancy between $\delta^{34}S_{sulfate}$ (our CAS vs. Paytan's barite) data were simply a temporal reconstruction issue, then the relationship between $\delta^{34}S_{sulfate}$ and $^{87}Sr/^{86}Sr$ should behave similarly in separate localities (e.g., Sr isotopes rebounding to pre-excursion values before S isotopes). The more likely scenario is that the $\delta^{34}S_{CAS}$ record during Interval 3 was influenced by either local environmental conditions and/or post burial alteration and therefore not representative of the primary marine global signal. The presence of scatter indicates that some degree of post-burial alteration has impacted the S isotope composition of CAS. However, we simply don't have enough information to determine if the Interval 3 $\delta^{34}S_{CAS}$ data represent local $\delta^{34}S_{sulfate}$ conditions at the time of carbonate precipitation or post-burial alteration of the primary marine signal (or both). Nevertheless, it is important to emphasize that the conclusions of this study are centered on the $\delta^{34}S_{CAS}$ results of Interval 2 (and their relationship with $^{87}Sr/^{86}Sr$), which track global $\delta^{34}S_{barite}$ results and therefore likely represent the secular evolution of marine $\delta^{34}S_{sulfate}$ in the Early Cretaceous.

Supplementary Figures

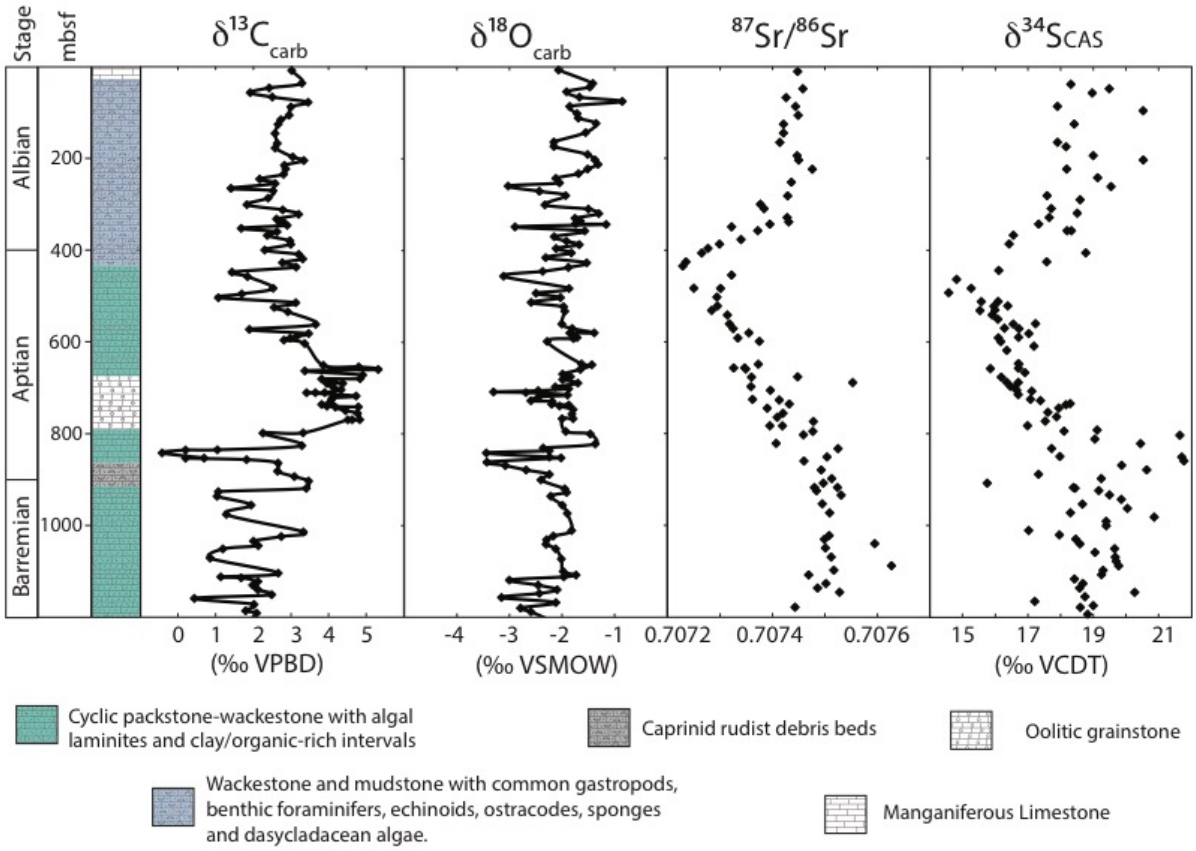

Figure S1. Stratigraphic column and geochemical results for rocks drilled at Resolution Guyot, Mid-Pacific Mountains (Site 866).

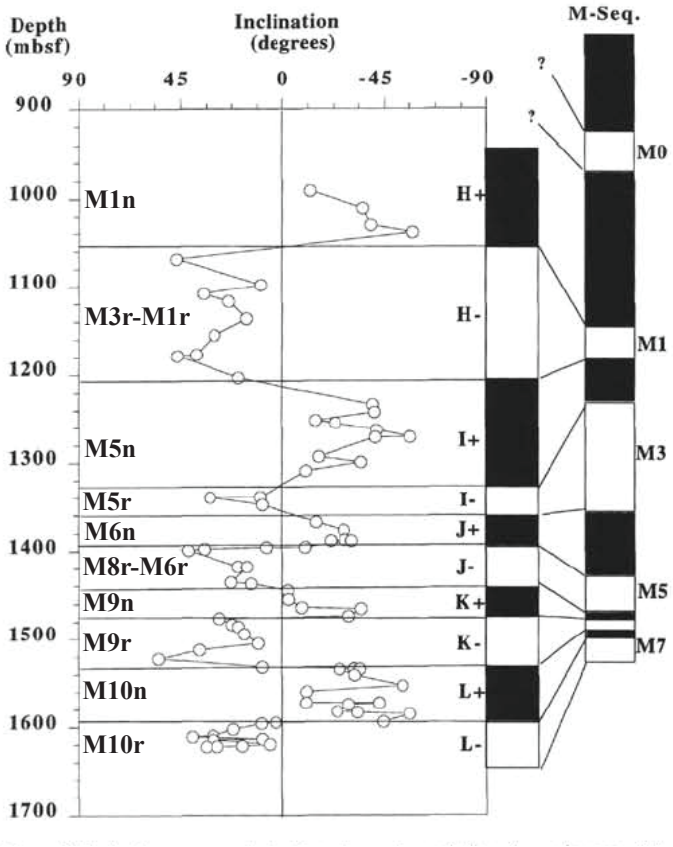

Figure S2. Magnetostratigraphic data (ref. 16) for ODP Hole 866A Resolution Guyot with initial M-series correlations (right side) and revised alignment with GTS2012 (left side).

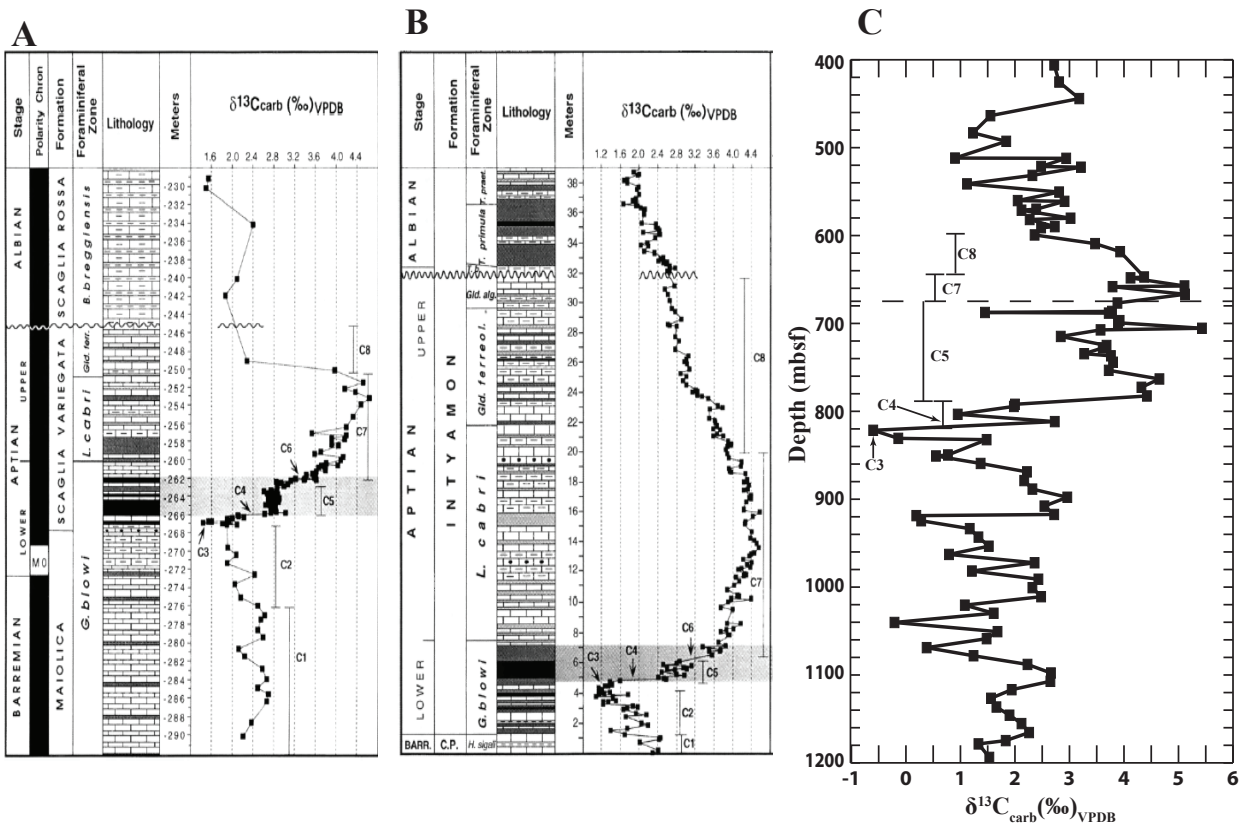

Figure 2. Lithologic logs and $\delta^{13}C_{carb}$ for the Cismon core (A) and Rotter Sattel section (B) from Menegatti et al., 1998. C) $\delta^{13}C_{carb}$ versus depth for Resolution Guyot ODP Hole 866A from this study.

Figure S3. Lithologic logs and $\delta^{13}C_{carb}$ for the Cismon core (A) and Rotter Sattel section (B)(Menegatti et al., 1998) compared to Site 866 $\delta^{13}C_{carb}$ results.

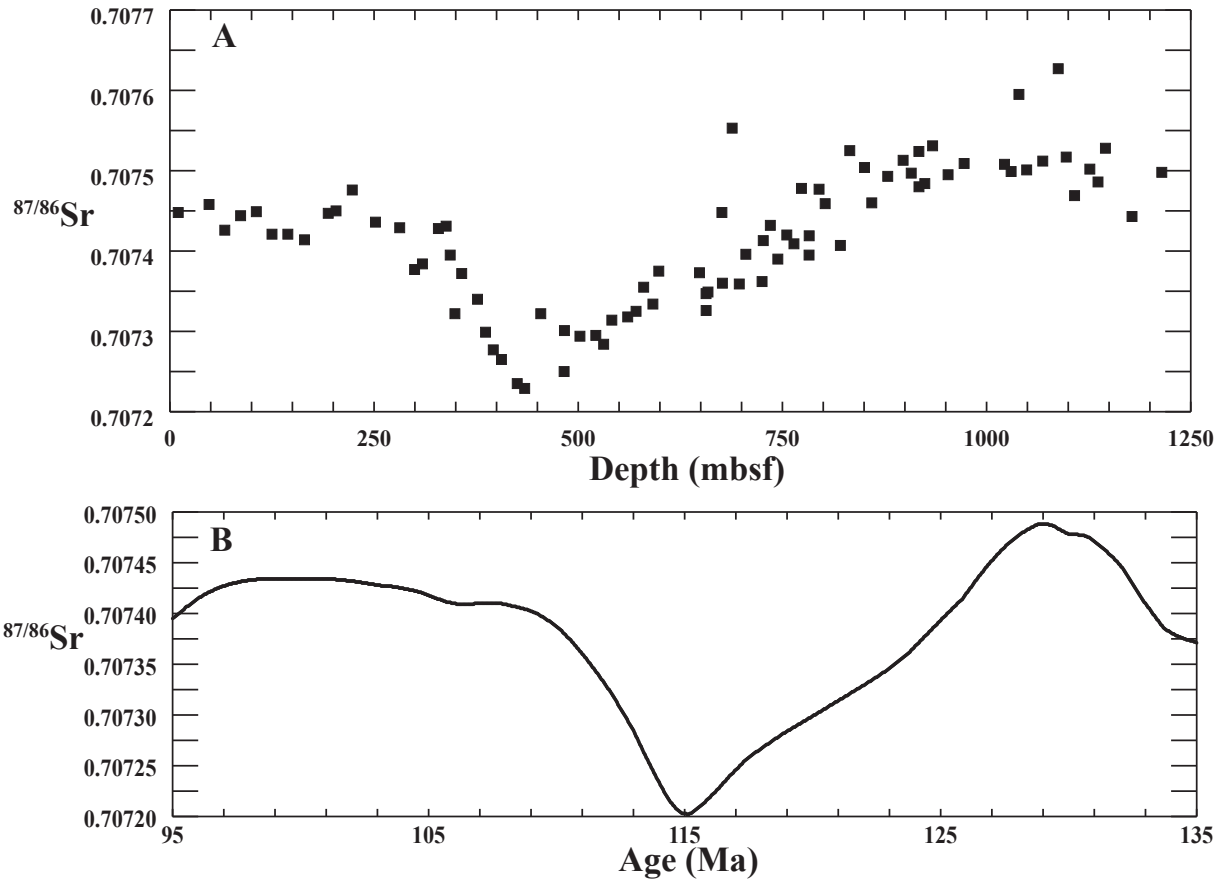

Figure S4. Strontium isotope stratigraphy for (A) Site 866A from Jenkyns et al., 1995 and (B) the GTS2012 LOWESS Fit 5 from McArthur, 2012.

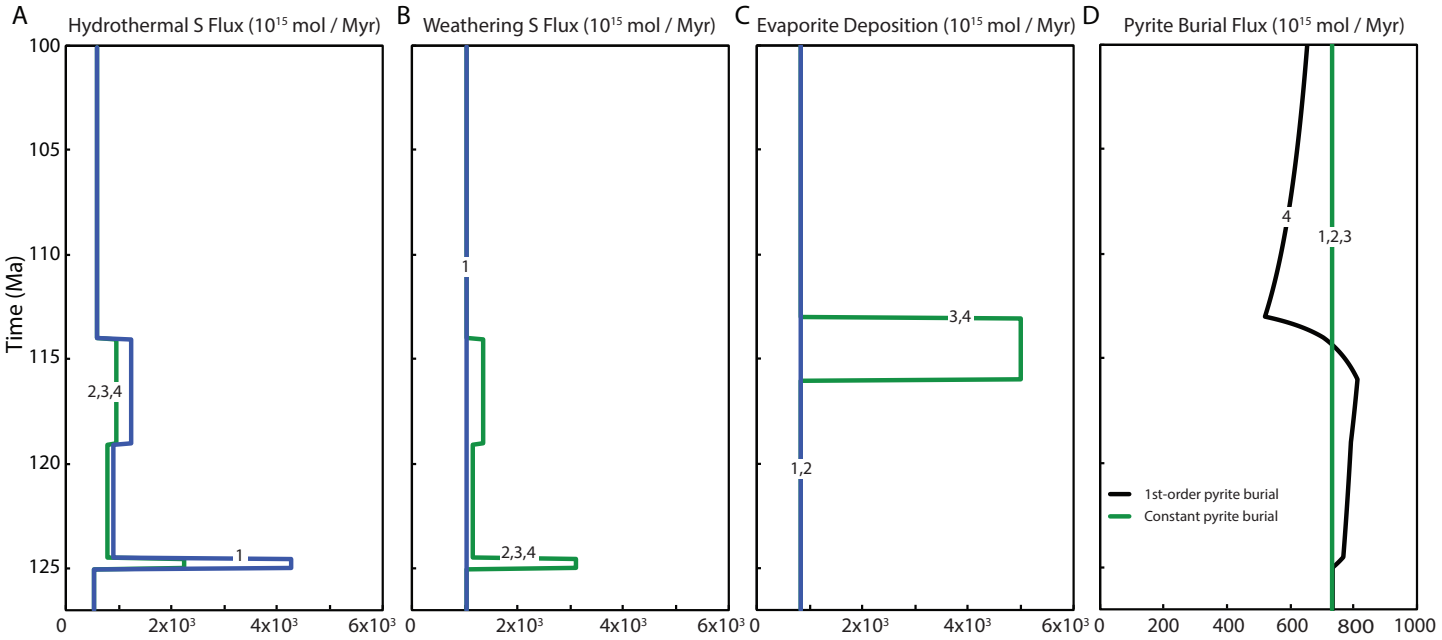

Figure S5. Sulfur cycle input and output fluxes under the various model scenarios. 1) Hydrothermal increase only - an initial large pulse of volcanism (8x increase in hydrothermal flux for 0.5Myr at 125Ma), followed by low-level volcanism (1.7x hydrothermal flux) for 5.5Myr, followed by a second smaller pulse of volcanism (2.3x hydrothermal flux for 5Myr). The hydrothermal flux is then maintained at 1.1x the original flux for the remainder of the simulation. 2) Increased weathering flux is included in the simulation: 4.2x hydrothermal + 3x weathering fluxes for 0.5Myr; 1.5x hydrothermal + 1.1x weathering for 5.5Myr; 1.8x hydrothermal + 1.3x weathering for 5Myr; 1.1x hydrothermal + 1x weathering for the remainder of the simulation. 3) Scenario 2, with an episode of evaporite deposition starting at 116Ma (6x evaporite flux for 3Myr). 4) Scenario 3, using a first-order pyrite burial flux.

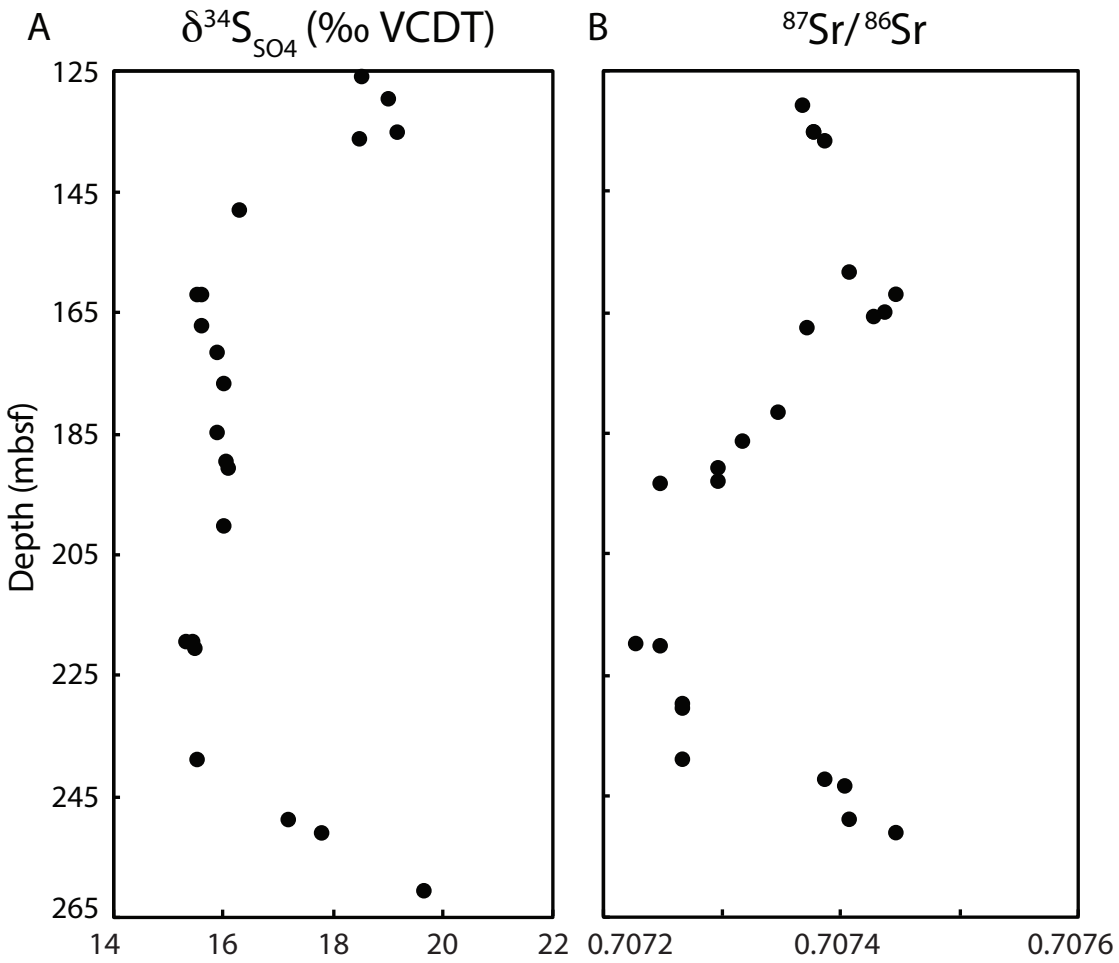

Figure S6. Sulfur ($\delta^{34}S_{barite}$, ‰VCDT – Paytan et al., 2004) and Strontium ($^{87}Sr/^{86}Sr$ – Mearon et al., 2003) isotope composition of marine barite, plotted with depth, from ODP site 766.

Supplementary Tables

Table S1. Key magnetostratigraphic, chemostratigraphic, and lithologic data for Early Cretaceous samples from ODP Hole 866A with new age assignments aligned with GTS2012.

Datum number	mbsf	data	Age Assignment	notes
13	130 ± 15	Benthic foraminifera stratigraphy	104.0 ± 0.5	Arnaud-Vanneau&Sliter, 1995 estimate with uncertainty Late Albian in core 15R-CC
12	343.23	$^{87/86}Sr$ = 0.707395 (normalized 0.707383)	109.4 ± 0.7	Albian-Cenomanian Plateau 0.707420±15 start 108.70 Ma; 866A before data plateaus
11	434.43	$^{87/86}Sr$ = 0.707229 (normalized 0.707217)	114.15 ± 0.55	Late Aptian min 0.707203 115.25-114.90 Ma GTS2012; 866A min on L. Aptian/E. Albian rise
10	599.3	$\delta^{13}C$ = 2.36‰	122.0 ± 0.5	End of C8 end of positive CIE associated with OAE1a; Menegatti et al., 1998 C8 ends within planktonic foraminifera G. algerianus
9	676.55	Lithologic boundary unit V to unit IV, SB17, and change from open marine to restricted Arnoud et al., 1995	Top 123.15 ± 0.425 Base 124.65 ± 0.425	suspected unconformity; suspect end of C5 missing C6 and most of C7 (1.5 of 1.94 Myr, Malinverno et al., 2010)
8	819 ± 2		125.4 ± 0.4	Start of positive CIE (C4 of Menegatti et al., 1998) associated with OAE1a/start of Selli Level equivalent
7	821.6	$\delta^{13}C$ = -0.59‰		C3 of Menegatti et al., 1998; peak negative excursion prior to start OAE1a
6	1054.2	H-/H+ magenetostratigraphic reversal Tarduno et al., 1995	128.32 ± 0.5	Assigned M3r-M1r/M1n Late Barremian
5	1218.7	I+/H- magenetostratigraphic reversal Tarduno et al., 1995	130.6 ± 0.5	Assigned M5n/M3r-M1r Early Barremian
4	1240 ± 2.5		130.8 ± 0.5	Hauterivian-Barremian boundary
3	1400.35	SB5 Arnaud et al., 1995 equivalent to Ha5 R/T megacycles GTS2012		Ha5 occurs within M7r
2	1475.3	K-/K+ magnetostratigraphic reversal Tarduno et al., 1995	133.30 ± 0.6	Assigned M9r-M9n boundary
1	1594.5	L-/L+ magnetostratigraphic reversal Tarduno et al., 1995	133.88 ± 0.6	Assigned M10r-M10n Valanginian-Hauterivian boundary

Table S2. Sedimentation rates used in the construction of the age model.

Sedimentation rate	Datums (Table 1)	Depth (mbsf)	Age (Ma)
S1	4-5	1218.7 – 1054.2	130.6 ± 0.5 – 128.32 ± 0.5
S2	5-7	1054.2 – 819 ± 2	128.32 ± 0.5 – 125.4 ± 0.4
S3	4-7	1218.7 – 819 ± 2	130.6 ± 0.5 – 125.4 ± 0.4
S4	3-7	1240 ± 2.5 – 819 ± 2	130.8 ± 0.5 – 125.4 ± 0.4
S5	7-8 base	819 ± 2 – 676.55	125.4 ± 0.4 – 124.65 ± 0.425
S6	8 top-10	676.55 – 599.3	123.15 ± 0.425 – 122.0 ± 0.5
S7	10-11	599.3 – 434.43	122.0 ± 0.5 – 114.15 ± 0.55
S8	11-12	434.43 – 343.23	114.15 ± 0.55 - 109.4 ± 0.7
S9	12-13	343.23 - 130 ± 15	109.4 ± 0.7 - 104.0 ± 0.5

Table S3. Initial steady-state conditions for Early Cretaceous sulfur and strontium cycles.

Sulfur			***Strontium***		
Parameter	Value	Units	Parameter	Value	Units
Initial R^{S}_{SW}	19.00	‰	Initial R^{Sr}_{SW}	0.7075	-
R^{S}_{H}	3.20	‰	R^{Sr}_{H}	0.7025	-
R^{S}_{W}	5.16	‰	R^{Sr}_{W}	0.7090	-
$\Delta^{34}S_{py}$	-31.00	‰	R^{Sr}_{D}	0.7072	-
F_{evap}	833.22	10^{15}*mol/myr*			
F_{py}	732.08	10^{15}*mol/myr*	F^{Sr}_{D}	12	10^{15}*mol/myr*
$F^{S}_{H}=hF^{Sr}_{H}$	533.25	10^{15}*mol/myr*	F^{Sr}_{H}	5.5	10^{15}*mol/myr*
$F^{S}_{W} = wF^{Sr}_{W}$	1035.35	10^{15}*mol/myr*	F^{Sr}_{W}	20.75	10^{15}*mol/myr*
Initial RT	5.3	*myr*	RT	2.4	*myr*

Supplementary References

Arnaud, H.M., Flood, P.G., and Strasser, A., 1995, Resolution Guyot (Hole 866A, Mid-Pacific Mountains): Facies evolution and sequence stratigraphy: Northwest Pacific atolls and guyots, in Proceedings of the Ocean Drilling Program, Scientific Results, v. 142, p. 133–159.

Arnaud-Vanneau, A., and Sliter, W.V., 1995, Early Cretaceous shallow-water benthic foraminifers and fecal pellets from Leg 143 compared with coeval faunas from the Pacific Basin, Central America, and the Tethys: Northwest Pacific atolls and guyots, in Proceedings of the Ocean Drilling Program. Scientific Results, v. 143, p. 537–564.

Bralower, T.J., *et al.*, 1999, The record of global change in mid-Cretaceous (Barremian-Albian) sections from the Sierra Madre, northeastern Mexico: J. Foraminifer. Res., v. 29, p. 418–437.

Gill, B. C., Lyons, T. W., Young, S. A., Kump, L. R., Knoll, A. H., and Saltzman, M. R., 2011, Geochemical evidence for widespread euxinia in the later cambrian ocean: Nature, v. 469, p.

80–83.

Gomes and Hurtgen, 2013, Sulfur isotope systematics of a euxinic, low-sulfate lake: Evaluating the importance of the reservoir effect in modern and ancient oceans: Geology, v. 41, p.663-666.

Herrle, J.O., Kobler, P., Friedrich, O., Erlenkeuser, H., and Hemleben, C., 2004, High-resolution carbon isotope records of the Aptian to Lower Albian from SE France and the Mazagan Plateau (DSDP Site 545): a stratigraphic tool for paleoceanographic and paleobiologic reconstruction: Earth and Planetary Science Letters, v. 218, p. 149–161.

Jenkyns, H.C., 1995, Carbon-isotope stratigraphy and paleoceanographic significance of the Lower Cretaceous shallow-water carbonates of Resolution Guyot, Mid-Pacific Mountains, in Proceedings of the Ocean Drilling Program, Scientific Results, v. 143, p. 99–104.

Jenkyns, H.C., Paull, C.K., Cummins, D.I., Fullagar, P.D., 1995, Strontium-isotope stratigraphy of Lower Cretaceous atoll carbonates in the Mid-Pacific Mountains, in: Proceedings of the Ocean Drilling Program, Scientific Results, v. 143, p. 89–97.

Jenkyns, H.C., and Strasser, A., 1995, Lower Cretaceous oolites from the mid-Pacific Mountains (Resolution Guyot, Site 866), in Proceedings of the Ocean Drilling Program, Scientific Results, v. 143, p. 111–118.

Jenkyns, H.C., and Wilson, P.A., 1999, Stratigraphy, paleoceanography, and evolution of Cretaceous Pacific guyots; relics from a greenhouse Earth: American Journal of Science, v. 299, p. 341–392.

Jones, C.E., and Jenkyns, H.C., 2001, Seawater Strontium Isotopes, Oceanic Anoxic Events, and Seafloor Hydrothermal Activity in the Jurassic and Cretaceous: American Journal of Science, v. 301, p. 112–149.

Luciani, V., Cobianchi, M., and Lupi, C, 2006, Regional record of a global oceanic anoxic event: OAE1a on the Apulia Platform margin, Gargano Promontory, southern Italy: Cretaceous Research, v. 27, p. 754–772.

Malinverno, A., Erba, E., and Herbert, T.D., 2010, Orbital tuning as an inverse problem: Chronology of the early Aptian oceanic anoxic event 1a (Selli Level) in the Cismon APTICORE: Paleoceanography, v. 25, doi:10.1029/2009PA001769.

McArthur, J.M., Howarth, R.J., and Shields, G.A., 2012, Strontium isotope stratigraphy. Geol. time scale, v. 1, p. 127–144.

Mearon, S., Paytan, A. and Bralower, T.J., 2003, Cretaceous strontium isotope stratigraphy using marine barite: Geology, v. 31, p.15-18.

Méhay, S. *et al.*, 2009, A volcanic CO_2 pulse triggered the Cretaceous Oceanic Anoxic Event 1a

and a biocalcification crisis: Geology, v. 37, p. 819–822.

Menegatti, A.P., *et al.*, 1998, High-resolution $\delta^{13}C$ stratigraphy through the Early Aptian 'Livello selli' of the Alpine tethys: Paleoceanography, v. 13, p. 530–545.

Ogg, J. G., 2012, *The Geologic Time Scale 2012*, eds. Gradstein, F.M., Ogg, J.G., Schmitz, M., and Ogg, G. (Elsevier), p. 85-113.

Ogg, J.G., Hinnov, L.A., 2012, *The Geologic Time Scale 2012*, eds. Gradstein, F.M., Ogg, J.G., Schmitz M, Ogg G. (Elsevier), p. 793-853.

Paytan A., Kastner M., Campbell D., Thiemens M.H., 2004, Seawater sulfur isotope fluctuations in the Cretaceous: Science, v. 304, p. 1663-1665.

Present, T.M., Paris, G., Burke, A., Fischer, W.W., and Adkins, J.F., 2015, Large carbonate associated sulfate isotopic variability between braciopds, micrite, and other sedimentary components in Late Ordovovician strata: Earth and Planetary Science Letters, v. 432, p. 187–198.

Pringle, M.S., and Duncan, R.A., 1995, Radiometric ages of basaltic lavas recovered at Sites 865, 866 and 869, in: Proceedings of the Ocean Drilling Program, Scientific Results, v. 143, p. 277–283.

Röhl, U., and Strasser, A., 1995, Diagenetic alterations and geochemical trends in early Cretaceous shallow-water limestones of allison and resolution guyots (sites 865 to 868), in Proceedings of the Ocean Drilling Program, Scientific Results, v. 143, p. 197-229.

Shipboard Scientific Party Leg 142, 1993, in *Proceedings of the Ocean Drilling Program, Initial Reports* (eds. Sager, W. W., Winterer, E. L. & V, F.), p. 181–271.

Strasser, A., Arnaud, H., Baudin, F., and Röhl, U., 1995, Small-scale shallow-water carbonate sequences of Resolution Guyot (Sites 866, 867, and 868), in Proceedings of the Ocean Drilling Program, Scientific Results, v. 143, p. 119–131.

Tarduno, J.A., Sager, W.W., and Nogi, Y., 1995, Early Cretaceous magnetostratigraphy and paleolatitudes from the Mid-Pacific Mountains: preliminary results bearing on guyot formation and Pacific plate translation: Northwest Pacific atolls and guyots, in Proceedings of the Ocean Drilling Program. Scientific results, v. 143, p. 395–398.

van de Schootbrugge, B., Föllmi, K.B., Bulot, L.G., and Burns, S.J., 2000, Paleoceanographic changes during the early Cretaceous (Valanginian–Hauterivian): evidence from oxygen and carbon stable isotopes: Earth and Planetary Science Letters, v. 181, p. 15–31.

Wilson, P.A., Jenkyns, H.C., Elderfield, H., and Larson, R.L., 1998, The paradox of drowned carbonate platforms and the origin of Cretaceous Pacific guyots: Nature, v. 392, p. 889–894.

Wortmann U.G., Chernyavsky B.M., 2007, Effect of evaporite deposition on Early Cretaceous carbon and sulphur cycling: Nature, v. 446, p. 654-656.

Wortmann, U.G., and Paytan, A., 2012, Rapidly variability of seawater chemistry over the past 130 million years: Science, v. 337, p. 334-336, doi: 10.1126/science.1220656.

ODP Leg 143, Site 866A, N21º 19.953', E174º 18.844'

Core-section, interval (cm)	Depth (mbsf)	Age (Ma)	Age uncertainty (σ)	$\delta^{34}S$ (VCDT)	$\delta^{13}C$ (VPDB)	$\delta^{18}O$ (VPDB)	87Sr/86Sr	Reference
6R-CC, 1-20	38.41	101.83	0.75	18.31	2.62	-1.64		This study
7R-CC, 30-35	48.1	102.06	0.73	19.48	2.37	-1.32		This study
8R-CC, 8-20	57.38	102.27	0.70	18.96	1.90	-2.10		This study
11R-CC, 1-10	86.51	102.96	0.62	17.90	2.21	-1.87		This study
12R-CC, 1-9	96.11	103.19	0.60	20.52	2.40	-2.08		This study
15R-CC, 8-15	125.08	103.87	0.52	18.41	2.67	-1.08		This study
19R-CC, 4-10	164.84	104.80	0.43	17.90				This study
20R-CC, 3-9	174.53	105.03	0.41	18.16	2.64	-1.74		This study
22R-CC, 5-12	193.85	105.49	0.38	18.99	2.99	-1.75		This study
23R-CC, 0-5	203.4	105.71	0.36	20.52	2.68	-1.52		This study
25R-1, 50-55	223.2	106.18	0.34	18.18	2.84	-1.98		This study
27R-CC, 3-10	242.03	106.62	0.33	19.13	1.59	-2.75		This study
29R-CC, 3-7	261.33	107.07	0.32	19.53	1.49	-3.10		This study
31R-1, 55-50	281.15	107.54	0.33	17.58	1.89	-2.17		This study
32R-CC, 20-25	290.1	107.75	0.34	18.59	1.94	-1.27		This study
34R-CC, 5-10	309.25	108.20	0.36	17.71	2.77	-0.96		This study
35R-1, 45-53	319.35	108.44	0.37	18.50	3.16	-1.20		This study
36R-1, 28-35	328.78	108.66	0.39	17.64	2.71	-1.58		This study
38R-1, 55-60	343.25	109.00	0.43	17.32	2.79	-1.71		This study
40R-CC, 30-42	357.6	109.83	0.37	18.26	2.73	-1.76		This study
41R-1, 34-40	367.34	110.39	0.32	16.55	2.70	-2.36		This study
43R-CC, 10-15	386.4	111.49	0.25	16.42	2.47	-2.78		This study
45R-CC, 23-27	405.83	112.60	0.20	18.76	2.72	-1.90		This study
47R-1 64-73	425.34	113.73	0.20	17.57	2.81	-1.63		This study
49R-CC, 15-23	444.15	114.71	0.20	16.10	3.18	-2.08		This study
51R-1, 22-28	463.62	115.62	0.18	14.81	1.55	-3.63		This study
53R-1 45-53	483.15	116.54	0.16	15.26	1.23	-3.62		This study
54R-1, 47-54	492.77	116.99	0.15	14.57	1.84	-3.10		This study
56R-1, 24-33	511.84	117.89	0.14	16.08	0.90	-3.02		This study
56R-1, 52-60	512.12	117.90	0.14	15.57	2.94	-3.12		This study
57R-1, 10-17	521.4	118.34	0.14	16.38	2.48	-1.82		This study
57R-1, 92-98	522.22	118.38	0.14	15.96	3.21	-2.97		This study
58R-1, 54-60	531.54	118.81	0.14	15.53	2.32	-3.01		This study
59R-1, 51-56	541.21	119.27	0.14	15.90	1.12	-2.01		This study
60R-1, 22-31	550.52	119.71	0.14	16.03	2.81	-2.74		This study
61R-1, 32-41	560.22	120.16	0.14	17.23	2.05	-2.17		This study

61R-1, 116-126	561.06	120.20	0.14	16.55	2.91	-2.20	This study
62R-1, 41-51	570.01	120.62	0.15	16.28	2.39	-2.67	This study
62R-2, 5-15	571.15	120.68	0.15	16.72	2.12	-2.40	This study
63R-1, 95-105	580.25	121.10	0.16		3.02	-2.53	This study
63R-2, 95-105	581.75	121.18	0.16	17.02	2.27	-1.69	This study
64R-1, 87-97	589.87	121.56	0.16	16.71	2.73	-1.90	This study
64R-2, 60-70	591.1	121.61	0.16	16.09	2.48	-1.92	This study
65R-1, 70-80	599.3	122.00	0.20	16.17	2.36	-1.43	This study
66R-1, 89-96	609.19	122.15	0.15	17.18	3.47	-1.74	This study
67R-1, 34-44	618.34	122.30	0.13	16.35	3.93	-1.68	This study
70R-1, 25-35	647.15	122.74	0.07	16.70	4.37	-1.97	This study
70R-2, 43-53	648.14	122.76	0.07	16.72	4.12	-1.38	This study
71R-1, 88-98	657.38	122.90	0.05	16.71	5.11	-0.98	This study
71R-2, 38-48	658.16	122.91	0.04	15.85	3.79	-1.44	This study
72R-1, 62-69	666.82	123.05	0.03	16.90	5.12	-1.53	This study
73R-1, 95-105	676.75	124.70	0.02	16.18	3.88	-2.63	This study
74R-1, 80-90	686.3	124.76	0.02		3.78	-2.54	This study
74R-3, 25-35	688.24	124.77	0.02	16.70	3.72	-2.22	This study
75R-2, 55-65	696.8	124.82	0.02	16.46	3.92	-2.49	This study
75R-4, 38-48	699.24	124.83	0.02	16.59	3.89	-2.18	This study
76R-1, 80-90	705.5	124.87	0.02	16.65	5.43	-2.69	This study
76R-2, 115-125	707.35	124.88	0.02	17.11	3.57	-3.71	This study
77R-1, 30-40	714.8	124.92	0.02	16.70	2.84	-2.22	This study
78R-1, 100-110	725.1	124.98	0.02	17.07	3.68	-2.49	This study
78R-3, 85-95	727.84	125.00	0.02	17.38	3.61	-2.63	This study
79R-1, 65-75	734.45	125.04	0.02	18.29	3.27	-2.22	This study
79R-3, 20-30	736.85	125.05	0.02	18.16	3.76	-2.32	This study
80R-1, 65-75	744.15	125.09	0.02	17.94	3.80	-2.08	This study
81R-1, 25-35	753.35	125.15	0.02	17.60	3.72	-1.67	This study
82R-1, 40-47	763.2	125.20	0.02	17.87	4.65	-2.07	This study
83R-1, 15-25	772.65	125.26	0.02	17.52	4.32	-2.43	This study
84R-1, 33-40	782.53	125.32	0.02	16.98	4.42	-2.43	This study
85R-1, 20-30	792	125.37	0.02	19.11	2.00	-2.22	This study
85R-2, 120-130	794.45	125.39	0.02	18.10	1.98	-1.58	This study
86R-2, 40-50	803.4	125.44	0.02	21.64	0.95	-1.47	This study
87R-1, 51-61	811.71	125.49	0.02	19.04	2.73	-1.73	This study
88R-1, 70-80	821.6	125.60	0.06	20.44	-0.60	-1.29	This study
89R-1, 15-25	830.75	125.72	0.06		-0.14	-2.94	This study
89R-2, 15-25	832.25	125.74	0.06	17.72	1.48	-3.00	This study
91R-1, 17-27	849.67	125.97	0.07	17.97	0.77	-2.60	This study

91R-2, 5-15	850.81	125.99	0.07	21.70	0.55	-2.31		This study
92R-1, 11-18	859.31	126.10	0.08	21.76	1.37	-2.86		This study
93R-1, 20-30	868.9	126.23	0.08	19.86	2.22	-3.24		This study
94R-1, 40-50	878.8	126.36	0.09	20.62	2.17	-2.91		This study
95R-1, 55-64	888.55	126.49	0.10	17.32	2.32	-2.29		This study
96R-1, 5-20	897.75	126.61	0.12	19.24	2.96	-2.64		This study
97R-1, 45-55	907.85	126.75	0.13	15.75	2.54	-2.87		This study
98R-1, 35-45	917.35	126.87	0.14	18.38	2.72	-2.39		This study
98R-2, 20-30	918.7	126.89	0.14	18.44	0.19	-2.49		This study
99R-1, 10-20	924	126.96	0.15	19.16	0.28	-2.22		This study
100R-1, 10-20	933.5	127.09	0.16	19.49	1.17	-2.58		This study
101R-1, 3-13	943.13	127.21	0.17	19.85	1.33	-2.33		This study
102R-1, 77-87	953.47	127.35	0.18	18.66	1.52	-2.52		This study
103R-1, 43-47	962.83	127.48	0.19	20.03	0.79	-2.28		This study
104R-1, 63-67	972.33	127.60	0.21	18.29	2.36	-2.37		This study
105R-1, 43-47	981.73	127.73	0.22	20.85	1.21	-2.53		This study
106R-1, 12-16	991.02	127.85	0.23	19.38	2.43	-1.86		This study
107R-1, 15-19	1000.65	127.98	0.24	19.39	2.32	-1.86		This study
108R-1, 73-77	1010.93	128.11	0.25	17.02	2.48	-1.75		This study
109R-1, 65-69	1020.55	128.24	0.27	17.96	1.08	-2.06		This study
110R-1, 15-19	1029.75	128.36	0.28	18.46	1.61	-1.88		This study
111R-1, 95-99	1040.25	128.50	0.29	18.58	-0.21	-2.25		This study
112R-1, 30-41	1050.7	128.64	0.31	19.64	1.68	-2.01		This study
113R-CC, 20-27	1058.7	128.74	0.30	19.04	1.48	-2.50		This study
114R-1, 70-77	1068.9	128.85	0.28	19.66	0.38	-2.50		This study
115R-1, 23-30	1078.13	128.95	0.26	19.69	1.24	-2.82		This study
116R-1, 48-55	1087.98	129.06	0.25	19.77	2.38	-2.34		This study
117R-1, 65-72	1097.75	129.17	0.23	19.29	2.66	-2.46		This study
118R-1, 40-47	1107.2	129.28	0.21	19.24	2.65	-2.37		This study
119R-1, 23-30	1116.73	129.38	0.19	18.42	1.94	-2.09		This study
120R-1, 40-47	1126.5	129.49	0.18	18.68	1.56	-2.60		This study
121R-1, 75-82	1136.45	129.60	0.16	18.57	1.66	-2.47		This study
122R-1, 35-42	1145.75	129.70	0.14	20.26	1.90	-1.47		This study
123R-1, 20-27	1155.3	129.81	0.13	18.74	2.12	-0.19		This study
124R-1, 70-77	1165.5	129.92	0.11	17.20	2.26	-1.01		This study
125R-1, 27-34	1174.67	130.02	0.10	18.99	1.83	-3.18		This study
125R-3, 110-117	1178.43	130.07	0.09	18.60	1.33	-3.53		This study
127R-1, 25-32	1193.75	130.24	0.08	18.82	1.53	-2.79		This study
3R-CC, 1-2	10.21	101.22	0.81				0.707448 *	
7R-CC, 14-15	47.94	102.10	0.71				0.707458 *	

9R-CC, 2-3	67.22	102.55	0.65	0.707426 *
11R-CC, 9-10	86.59	103.01	0.60	0.707444 *
13R-CC, 3-4	105.83	103.45	0.55	0.707449 *
15R-CC, 2-3	125.02	103.90	0.51	0.707421 *
17R-CC, 2-3	144.42	104.36	0.46	0.707421 *
19R-CC, 7-8	164.87	104.83	0.42	0.707414 *
22R-CC, 8-9	193.88	105.51	0.37	0.707447 *
23R-CC, 3-4	203.43	105.73	0.35	0.70745 *
25R-1, 61-62	223.31	106.20	0.33	0.707476 *
28R-CC, 9-11	251.69	106.86	0.32	0.707436 *
31R-1, 81-82	281.41	107.56	0.33	0.707429 *
33R-CC, 12-13	299.62	107.98	0.35	0.707377 *
34R-CC, 4-6	309.24	108.21	0.36	0.707384 *
36R-1, 27-28	328.77	108.66	0.39	0.707428 *
37R-1, 24-26	338.24	108.88	0.41	0.707431 *
38R-1, 53-54	343.23	109.00	0.50	0.707395 *
39R-2, 41-42	349	109.33	0.41	0.707322 *
40R-CC, 1-3	357.31	109.81	0.37	0.707372 *
42R-CC, 7-8	376.67	110.93	0.29	0.70734 *
43R-CC, 21-22	386.51	111.49	0.25	0.707299 *
44R-CC, 7-8	395.97	112.04	0.22	0.707277 *
45R-CC, 38-40	405.98	112.61	0.20	0.707265 *
47R-1, 60-62	425.3	113.72	0.20	0.707235 *
48R-1, 3-5	434.43	114.25	0.25	0.707229 *
50R-CC, 42-44	454.12	115.18	0.19	0.707322 *
53R-1, 1-5	482.71	116.52	0.16	0.70725 *
53R-1, 41-44	483.11	116.54	0.16	0.707301 *
55R-CC, 18-19	502.08	117.43	0.15	0.707294 *
57R-1, 22-24	521.52	118.34	0.14	0.707295 *
58R-1, 12-13	531.12	118.80	0.14	0.707284 *
59R-1, 44-46	541.14	119.27	0.14	0.707314 *
61R-1, 68-69	560.58	120.18	0.14	0.707318 *
62R-1, 120-122	570.8	120.66	0.15	0.707325 *
63R-82-84	580.12	121.10	0.16	0.707355 *
64R-2, 93-95	591.43	121.63	0.17	0.707334 *
65R-1, 3-6	598.63	121.97	0.17	0.707375 *
70R-2, 76-80	648.47	122.76	0.06	0.707373 *
71R-1, 12-14	656.5	122.89	0.05	0.707347 *
71R-1, 10-11	656.6	122.89	0.05	0.707326 *
71R-2, 110-112	658.88	122.93	0.04	0.707349 *

73R-1, 13-16	675.92	123.19	0.02	0.707448 *
73R-1, 72-74	676.52	123.20	0.02	0.70736 *
74R-3, 48-50	688.47	124.77	0.02	0.707553 *
75R-2, 94-95	697.19	124.82	0.02	0.707359 *
76R-1, 53-56	705.23	124.87	0.02	0.707396 *
78R-1, 99-100	725.09	124.98	0.02	0.707362 *
78R-2, 105-111	726.54	124.99	0.02	0.707413 *
79R-1, 141-143	735.21	125.04	0.02	0.707432 *
80R-1, 90-92	744.4	125.10	0.02	0.70739 *
81R-3, 30-31	755.38	125.16	0.02	0.70742 *
82R-1, 133-135	764.13	125.21	0.02	0.707409 *
83R-1, 81-82	773.31	125.26	0.02	0.707478 *
84R-1, 42-45	782.62	125.32	0.02	0.707395 *
84R-1, 58-60	782.78	125.32	0.02	0.707419 *
85R-3, 13-15	794.88	125.39	0.02	0.707477 *
86R-1, 86-89	802.36	125.43	0.02	0.707459 *
88R-1, 8-9	820.98	125.59	0.05	0.707407 *
89R-2, 38-39	832.48	125.74	0.06	0.707525 *
91R-1, 104-107	850.54	125.98	0.07	0.707504 *
92R-1, 22-24	859.42	126.10	0.08	0.70746 *
94R-1, 57-60	878.97	126.36	0.09	0.707493 *
96R-1, 11-13	897.81	126.61	0.12	0.707513 *
97R-1, 33-36	907.73	126.74	0.13	0.707497 *
98R-1, 11-16	917.11	126.87	0.14	0.707524 *
98R-1, 20-23	917.2	126.87	0.14	0.70748 *
99R-1, 46-49	924.36	126.96	0.15	0.707484 *
100R-1, 51-54	933.91	127.09	0.16	0.707531 *
102R-1, 16-20	952.86	127.34	0.18	0.707495 *
104R-1, 81-83	972.51	127.60	0.21	0.707509 *
109R-2, 89-91	1021.93	128.26	0.27	0.707508 *
110-1, 45-48	1030.05	128.37	0.28	0.707499 *
111R-1, 30-33	1039.6	128.49	0.29	0.707595 *
112R-1, 19-21	1049.09	128.62	0.30	0.707501 *
114R-1, 59-62	1068.79	128.85	0.28	0.707512 *
116R-1, 22-27	1087.72	129.06	0.25	0.707627 *
117R-1, 40-43	1097.5	129.17	0.23	0.707517 *
118R-1, 94-96	1107.74	129.28	0.21	0.707469 *
120R-1, 34-38	1126.44	129.49	0.18	0.707502 *
121R-1, 73-75	1136.43	129.60	0.16	0.707486 *
122R-1, 11-13	1145.51	129.70	0.14	0.707528 *

Jenkyns, H.C., Paull, C.K., Cummins, D.I., Fullagar, P.D., 1995, Strontium-isotope stratigraphy of Lower Cretaceous atoll carbonates in the Mid-Pacific Mountains, in: Proceedings of the Ocean Drilling Program, Scientific Results, v. 143, p. 89–97.